Analyzing laser-plasma interferograms with a Continuous Wavelet Transform Ridge Extraction technique

P. Tomassini[1*], M. Borghesi[3], M. Galimberti[1,2]
A. Giulietti [1], D. Giulietti[1,2], O. Willi[4] and L.A. Gizzi[1]

[1]Intense Laser Irradiation Laboratory - IFAM,
CNR Area della Ricerca di Pisa (Italy)

[2] Dipartimento di Fisica Universita' di Pisa (Italy) and I.N.F.M sez. di Pisa

[3] The Queen's University, Belfast (UK)

[4] Blackett Laboratory
Imperial College of Sciences, Technology and Medicine, London (UK)

Main contact E-mail address: tomassini@ifam.pi.cnr.it

February 6, 2001

Abstract

Laser-plasma interferograms are currently analyzed by extracting the phase-shift map with FFT techniques (K.A.Nugent, Applied Optics **18***, 3101 (1985)). This methodology works well when interferograms are marginally affected by noise and reduction of fringe visibility, but it can fail in producing accurate phase-shifts maps when dealing with low-quality images.*

In this paper we will present a novel procedure for the phase-shift map computation which makes an extensive use of the Continuous Wavelet Transform. We compare the performances of the new technique ("Interferogram Analysis by Continuous wavelet trasform Ridge Extraction") with the standard FFT-based technique.

We will show that the new procedure works better than the FFT-based one in two main aspects: it is considerably more robust particularly in the case of strongly noisy fringe patterns and it is more accurate since it can resolve local inhomogeneties with lower perturbations in the phase-shifts map. We then claim that this new technique will help us in improving the characterization of local inhomogeneities in the plasma density.

1 Introduction

Interferometric techniques are widely used to characterize the optical properties of a variety of media. An important class of applications concerns the investigation of the density distribution of plasmas produced by high intensity laser-matter interactions. In recent years various interferometer schemes have been developed and successfully applied to the characterisation of the wide range of plasma condition which can be achieved in laser-plasma experiments, from the long-scalelength underdense plasma generated by laser explosion of a thin foil target to the steep, denser plasma generated by short pulse inter-

action with a solid target. All these schemes make use of a so-called probe beam which consists of a laser pulse which probes the plasma at a given time. In one of these schemes, referred to as "modified Nomarski interferometer" [1][2] [3], a portion of this beam propagates through the plasma and carries the phase shift information. Finally this portion of the beam is made to interfere with an unperturbed portion to generate a fringe pattern. The fringe pattern must be then analysed to obtain the two-dimensional phase-shift which contains the physical information on the plasma. Then, provided that appropriate symmetry conditions are satisfied, inversion techniques can be applied to the phase shift map to obtain the density profile.

The simplest way of reading a fringe pattern consists in building a grid over the pattern and in measuring, for each position on the grid, the number of fringe jumps with respect to the unperturbed fringe structure. This procedure is very simple and can be performed manually. However, the amount of information which can be extracted in this way is very limited due to the small number of grid points that can be employed.

In 1982 a novel fringe analysis technique was proposed [4] in which the phase extraction was carried out using a procedure based upon Fourier transform. This technique allows the information carried by the fringe pattern on the film to be decoupled by spatial variations of the background intensity as well as by variations in the fringe visibility, provided that the scalelength of such perturbations is large compared to the fringe separation. A few years later this FFT technique was applied for the first time to laser-produced plasmas [5]. More recently the technique was extensively applied by our group to the analysis of long-scalelength underdense laser-plasmas [6]. In recent years great advances in the interferometry of laser-plasmas has been achieved using subpicosecond probe pulses. The use of short pulses as probes has the great advantage of reducing dramatically the fringe-smearing effect due to the motion of the plasma during the probe pulse. This fact allowed to investigate short-lived phenomena in the propagation of ultra-short laser pulses through plasmas [7].

The extensive use of the FFT based technique carried out by our group has shown that this technique is in general fast and very effective. In some circumstances however, reduction of fringe visibility, non uniform illumination, noise and the presence of local image defects make the FFT based analysis technique unstable and the results are not fully satisfactory because of the presence of unphysical phase jumps. In addition, the phase-shift map is generally noisy and small non-uniformities with low departure from the density background are unlikely to be detected, so *more robust and accurate* analysis techniques are needed.

In this paper we show that Continuous Wavelet Transforms can be successfully applied to the analysis of interferograms resulting in a more flexible and reliable than the FFT based technique. To our knowledge, this is the first time that a Continuous Wavelet Transform approach is applied to fringe pattern analysis and in particular to interferometric analysis in laser-produced plasmas.

In section 2 we will shortly introduce the Continuous Wavelet Transform (CWT), stressing its remarkable properties of good space-scale analyzer.

In section 3 we introduce our *IACRE*, "Interferogram Analysis by Continuous wavelet trasform Ridge Extraction" tool for interferograms analysis and we compare its robustness and sensibility performances with the FFT-based method.

Section 4 is devoted to comments and further activity description.

2 A short introduction to Continuous Wavelet Analysis

2.1 The need for a time-frequency analysis

The Continuous Wavelet Transform is a tool to obtain a representation of signal s which is intermediate between the "real time" description $s = s(t)$ and the "spectral" description $\hat{s} = \hat{s}(\omega)$, so that it is a very powerful tool to obtain a space-scale (or time-frequency) description of a sequence of data.

The need of a time-frequency (or "space-scale", in this paper we will utilize either the label t or x for the representation of a signal) description of a sequence is much strong in cases of well-localized events in the signal or when the signal represents a sum of

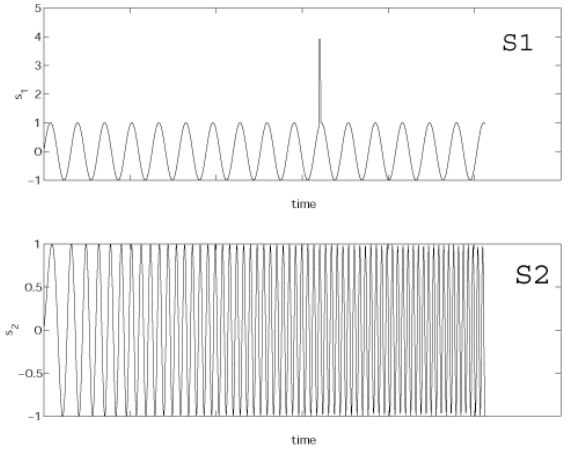

Figure 1: *The signal s_1: a sinusoid with a well localized event. The signal s_2: a frequency-modulated sinusoid.*

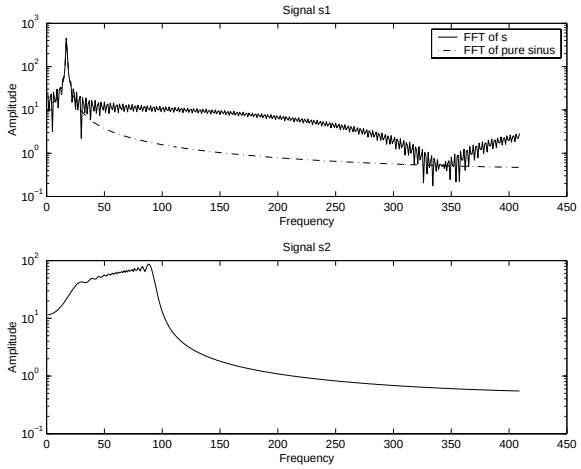

Figure 2: *Fast Fourier Transform of s_1 and s_2. The dashed line in the top frame represents the module of the FFT coefficients for a pure sinus.*

frequency-modulated components (as for each section of an interferogram image, see section 4). Consider for example the two signals(see Fig. 1):

$$\begin{aligned} s_1 &= \sin\left((2\pi t) + a\,\delta(t-t_0)\right), \\ s_2 &= \sin\left((2\pi t)(1+b\sqrt{t})\right). \end{aligned} \tag{2.1}$$

Apart from the presence of a "jump" at time t_0, the first signal is a pure sinusoid. The second signal, instead, is a frequency-modulated sinusoid. What's about FFT coefficients? What can be learned from them? Let's look Fig. 2; the module of the FFT coefficients for s_1 tells us that the main component of the signal is a sinusoid (the sharp peak), but nothing can be inferred about the departure of the signal from a pure sine: neither if such departure is periodic nor, if not, if it is well localized in time (and consequently at which time is concentrated). The modulus of the FFT coefficients for s_2 are even less helpful in suggesting us the structure of the signal: a broad band of frequencies is present and no main frequency can be found. These simple examples show that a "full spectral" analysis could be unsatisfactory if we are interested in the knowledge of both the spectral contain and time structure of a signal.

The obvious step that can be made to overcome the lack of time sensitivity is the introduction of a sequence of windows of a given width and centered at different times: for each window the FFT of the signal is computed and a partial time resolution is obtained. These techniques are called "Short-Time Fourier Transform" or "Windowed Fourier Transform" or "Gabor Transform" [9]. The Gabor Transform is currently used in many context but is not considered by the signal-processing community a "full analysis tool". This is because the number of oscillations of each sinus in the window depends on the frequency and consequently the spectral and spatial resolutions should be optimized (by tuning the window length) only in a narrow band.

From the early 80's, with the introduction of the Wavelet Transform, a satisfying time-frequency analysis tool is available [10] [11] [12].

2.2 The Continuous Wavelet Transform

To introduce the Wavelet Transform, let us first define notations for the Fourier Transform. For a signal $s \in L^1(\mathcal{R}) \cap L^2(\mathcal{R})$ the Fourier coefficients, that is the scalar product between the signal and the infinitely oscillating terms $e_\omega = e^{-i\,\omega t}$:

$$\hat{s}(\omega) \equiv < e_\omega | s > = \int_{-\infty}^{\infty} dt e^{-i\,\omega t} s(t) \tag{2.2}$$

form a complete basis of the space to which s belongs and an inverse Fourier transform can be applied to $\hat{s}(\omega)$ to recover s: $s(t) = \int_{-\infty}^{\infty} d\frac{\omega}{2\pi} e^{i\,\omega t}\hat{s}(\omega)$.

Let us introduce a function $\Psi(t)$ called *Mother wavelet*. Now, instead of decomposing the signal s as a sum of the pure oscillating terms e_ω (*Fourier*

Transform), we build a decomposition of s **in terms of the base of all the translated** (with parameter b) **and scaled** (with parameter a) Ψ (*Continuous Wavelet Transform*). The basis of the Continuous Wavelet Transform (*CWT*) is then a two-parameter family of functions

$$\Psi_{a,b}(t) \equiv \frac{1}{a}\,\Psi\left(\frac{(t-b)}{a}\right). \qquad (2.3)$$

The choice of the Mother Wavelet used to build the analyzing base is quite free (with a restriction that will be shown below) and must be adapted to the actual information that should be extracted from the signal. This is an important topics that the reader may deepen with the help of reference [11].

Once the two-parameter base has been built, one can compute the CWT coefficients as

$$\begin{aligned} W_s(a,b) \quad &\equiv \quad < \Psi_{a,b}|s > \qquad (2.4)\\ &= \quad \int_{-\infty}^{\infty} dt \frac{1}{a}\overline{\Psi\left(\frac{(t-b)}{a}\right)}\, s(t),\\ (\quad [a,\,b] \quad &\in \mathcal{R},\ a>0\ ) \end{aligned}$$

or, with the help of Fourier Transform, as [11]

$$W_s(a,b) = \frac{1}{2\pi}\int_{-\infty}^{\infty} d\omega\,\overline{\hat{\Psi}}(a\,\omega)e^{i\,\omega\,b}\hat{s}(\omega)\,. \qquad (2.5)$$

If the Mother Wavelet Ψ has zero mean (*admissibility condition*), then an inversion algorithm can be applied [12]; the simpler procedure to recover the signal s from its Wavelet transform is the so-called "Morlet inversion formula"

$$s(t) = \frac{1}{k_\Psi}\int_0^{\infty} W_s(a,b)\frac{da}{a} \qquad (2.6)$$

where it is assumed that

$$k_\Psi = \int_0^{\infty} \overline{\hat{\Psi}(a\xi)}\frac{da}{a}$$

is finite, nonzero and independent on ξ.

In the subset of admissible wavelets, "Morlet-family" wavelets are largely used in studying signals with strong components of pure sinus or modulated sinusoids. The Morlet base has the form

$$\Psi(t) = e^{i\,\omega_0 t}\ e^{-(t/\tau)^2}\,, \qquad (2.7)$$

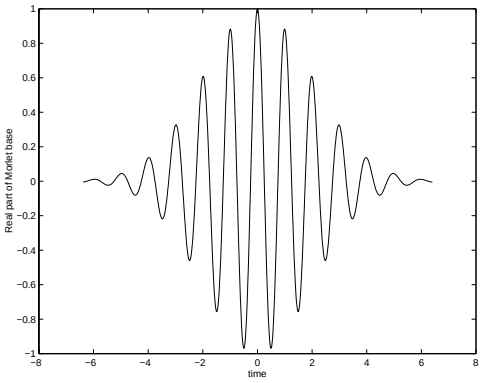

Figure 3: *The real part of Morlet Mother Wavelet.* $\omega_0 = 2\pi; \tau = 4$.

where the parameters ω_0 and τ control the peak frequency and the width of the wave respectively. The product $\omega_0 \times \tau$ *controls the time and spectral resolution of the Wavelet decomposition*: a large τ corresponds to a long wave (high spectral resolution and low temporal resolution) while a small τ produces an "event based" analysis (low spectral resolution and high temporal resolution).

We now face the problem of a numerical computation of the Wavelet coefficients map $W_s(a,b)$. For a sequence of N samples s_i; $i = 1...N$ of s, the translation parameter b (which controls the central position of the wave envelope) can be sampled in a straightforward way: $b \to b_i$; $i = 1...N$. The scaling parameter a (which controls the characteristic scale of the wave) may be sampled in two main ways:

- **Linear frequency sampling:** $\frac{2\pi}{a_j} = k_1 + \frac{j}{M}k_2 - k_1;\ j = 1...M$, where k_1 and k_2 are the lower and upper wave vectors which are analyzed.
- **Natural sampling or Log sampling:** $a_j = 2^{-j/N_v}\ j = 1...M$, where N_v is the "number of voices per octave" parameter. Each a_j is called "voice" and, in the case $N_v = 12$, Log sampling exactly corresponds to the spectral sampling of musical tones in the "tempered scale" introduced by J.S. Bach.

The Log sampling of CWT coefficients in the Morlet basis is very useful when the spectral content of the signal is the main information to be extracted, because it provides a good compromise between spatial and spectral resolution. As the reader can easily

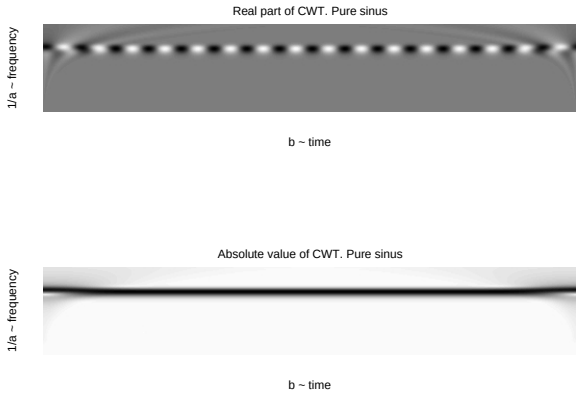

Figure 4: *The real part and absolute value CWT maps of a pure sinus with Morlet Mother Wavelet.*

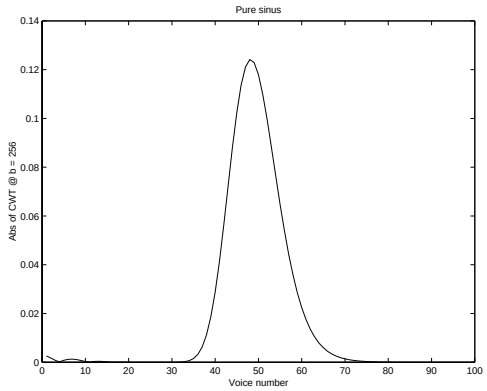

Figure 5: *The absolute value CWT map of a pure sinus of Morlet Mother Wavelet: a zoom @b constant.*

check, the spectral resolution at each voice is proportional to the peak frequency of the voice $\left(\frac{\omega_o}{a}\right)$ so that the relative spectral uncertainty $\frac{\Delta f}{f}$ is constant along the a axes.

To familiarize with the CWT map, we compute the CWT coefficients of a pure sine signal. Figure Fig. 4 shows both the real part and the absolute value of CWT coefficients in the Log sampling ($N_v = 24$). In these figures CWT maps are organized with "frequencies" increasing from the top to the bottom. The absolute value of CWT map is almost zero, apart from a thin horizontal band centered at a scale corresponding to the input signal frequency: CWT may be a good spectral analyzer even for perfectly periodic signals (see also Fig. 5 in which a "zoom", that is a section of the absolute value of CWT map at $b = const.$, is shown).

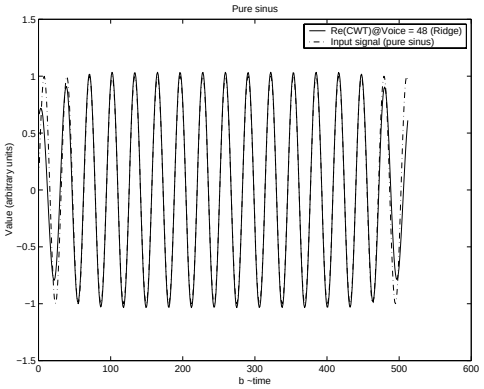

Figure 6: *The sequence of real part of CWT map of a pure sinus with Morlet Mother Wavelet @ Ridge.*

The real part of CWT map shows a second important feature of CWT with Morlet (or generally with progressive) basis: $\mathcal{R}(W_s)$ is almost constant, apart from the thin band centered at the signal frequency. The sequence

$$R_s(b) \equiv \mathcal{R}(W_s)(b, a_R(b)) \tag{2.8}$$

where for each b^* $a_R(b^*)$ is the voice corresponding to a local maximum of the zoom of $abs(CWT)$ at $b = b^*$, well reproduces the input signal itself, as is shown in Fig. 6.

The sequence (ore more generally the sequences when more complex signals are analyzed) 2.8 is called *the Ridge of CWT map* and represents the subset of CWT map where most of the "energy" is contained. To familiarize with Ridge properties, let us consider a signal of the form:

$$s(t) = A(t)\ \cos(\phi(t)) \tag{2.9}$$

where $A(t)$ is assumed be slowly varying with respect to the oscillations, that is

$$\frac{1}{A}\frac{dA}{dt} << \phi' .$$

If Ψ is a progressive Wavelet, then with straightforward computations including "stationary phase methods" we have (see [14] and [13])

$$W_s(a,b) \approx \frac{1}{2} A(b) e^{i\,\phi(b)}\, \overline{\hat{\Psi}(a\phi'(b))} . \tag{2.10}$$

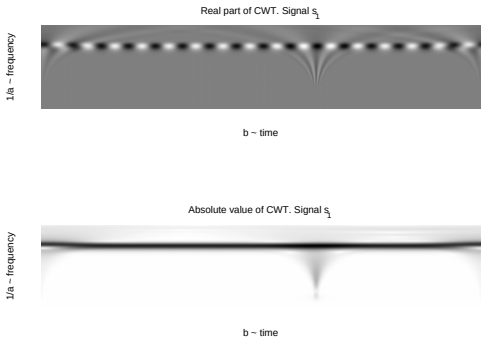

Figure 7: *The real part and absolute value CWT maps of a signal s_1 with Morlet Mother Wavelet.*

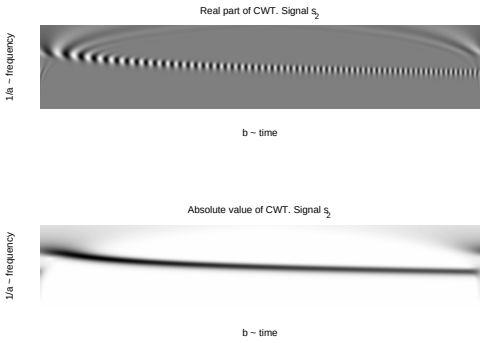

Figure 8: *The real part and absolute value CWT maps of a signal s_2 with Morlet Mother Wavelet.*

Since $\hat{\Psi}$ is centered at $\omega = \omega_0$, $\hat{\Psi}(a\phi'(b))$ is not negligible if

$$a \approx a_R(b) \equiv \frac{\omega_0}{\phi'(b)} \tag{2.11}$$

which means that the energy of the CWT map is localized around a thin curve, the *Ridge* curve. To conclude, it is interesting to note that the "instantaneous frequency", that is the time derivative of the phase $\phi(t)$

$$\Omega(t) \equiv \phi'(t)\,,$$

can be easily extracted from the Ridge curve: for each b, as corollary of (2.10), $a_R(b)$ is linked to Ω as

$$\Omega(b) = \frac{\omega_0}{a_R(b)}\,.$$

Let us now compare FFT and CWT analysis of signals s_1 and s_2 (Fig. 1). The CWT map of signal s_1 is reproduced in Fig. 7. Unlike FFT map, in Fig. 7 is evident that the signal s_1 is something like a pure sine of measurable frequency plus some localized event at a detectable time t_0. In addition, since the shape of the CWT of the most localized inputs are well known, on can easily recognize that the event is similar to a *delta* shot.

The analysis of the CWT map of signal s_2 (see Fig. 8) is more interesting for our scope. The map shows a single ridge, then a single frequency-modulated signal is present with instantaneous frequency $\Omega(b)$ increasing with time. The Ridge sequence $R_{s_2}(b) \equiv \mathcal{R}(W_{s_2})(b, a_R(b))$ is shown in Fig. 9 and it is compared with the input signal s_2 itself. Apart from boundary-generated errors, the Ridge sequence well reproduces the input signal; *this means that the Ridge*

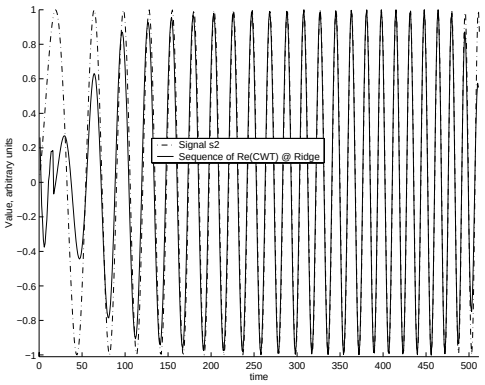

Figure 9: *The sequence of real part of CWT map of signal s_2 with Morlet Mother Wavelet @ Ridge*

CWT sub-map succeed in capturing the signal characteristics as for example instantaneous intensity, phase and frequency. This is the main characteristic of CWT analysis which will constitute the core of the *IACRE* interferograms analysis (see next section).

2.3 Noisy data

We now face one of the most relevant problems in signal processing: the identification and (eventually) the parameters estimation of a noisy signal. Ridge analysis of CWT map plays a rising role in signal processing, especially in the search of non-stationary signals with a very low SNR ratio (see [15] and references therein).

To explore CWT performances in the presence of noisy data, we add gaussian noise to signal s_2 (see Fig. 10) and compute the CWT map (Fig. 11). The

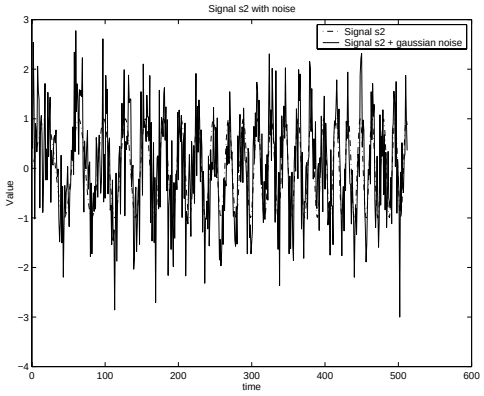

Figure 10: *The signal s_2 with gaussian noise added (SNR = 0.8) .*

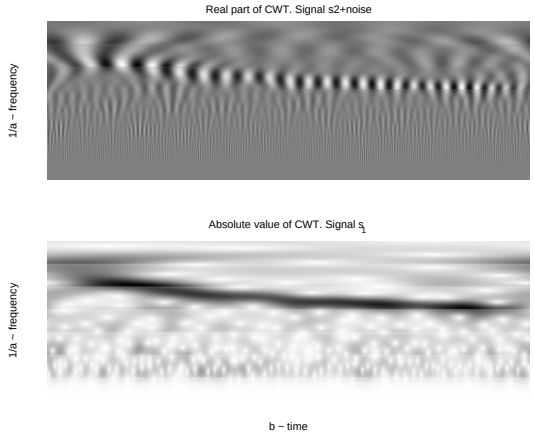

Figure 11: *The real part and absolute value CWT maps of a signal $s_2 + noise\,(SNR = 0.8)$ with Morlet Mother Wavelet.*

presence of noise (in this case at SNR = 0.8) does not destroy the Ridge structure and the resulting Ridge detection gives rise to the sequence $R_{s_2+noise}(b) \equiv \mathcal{R}(W_{s_2+noise})(b, a_R(b))$ reproduced in Fig. 12. As it is clear in Fig. 12 the Ridge sub-map well captures the "true" input signal even in the presence of a quite strong noise. This is the reason why one of the applications of Wavelet Transform is the denoising of one dimensional data. *To conclude, we stress that the extraction Ridge sequence of the CWT map constitutes a complete and robust method to* **denoise and identify** *a sequence made by (eventually a sum of) frequency-modulated harmonic terms.*

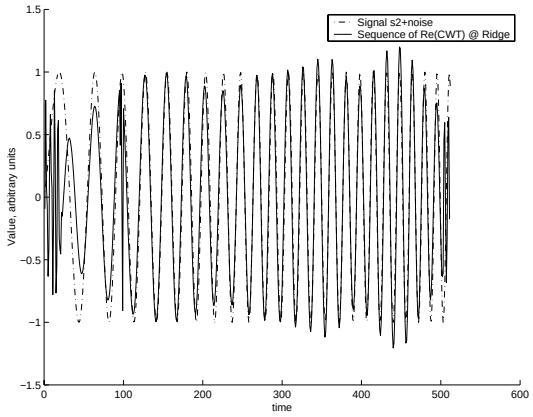

Figure 12: *The sequence of real part of CWT map of signal s_2+noise with Morlet Mother Wavelet @ Ridge (SNR = 0.8) .*

3 Comparison between the FFT-based and the *IACRE* methods to extract phase-shift map from interferograms

3.1 The FFT-based method for phase-shift estimation

The extraction of phase-shift map, that is the computation for each pixel of an interferogram image of the phase-shift with respect to a unperturbed wave profile, is usually performed with the help of Fast Fourier Transform (FFT-based method). Consider for example the interferogram of Fig. 13, whose gray-level map be $I(z, x)$ and for each Z build the sequence $s_Z \equiv I(z = Z, x)$ (that is a horizontal section of the figure). For a unperturbed interferogram image the sequences s_Z should be similar to pure oscillating terms plus noise and (eventually) a slowly varying background. If the departure of such a behaviour is identified as a local frequency modulation of the oscillating term, then the phase-shift $\delta\phi(z, x)$ can be easily computed as the difference between the "true" phase at each x position and the corresponding phase of the not-perturbed sequence. Figure 14 shows a sequence s_Z for $Z = 400$ (the middle of the frame). The behaviour of s_Z can be identified as a frequency-modulated oscillation with local frequency $\Omega(x)$ increasing with x, plus noise and slowly rising background. In addition, the amplitude of oscilla-

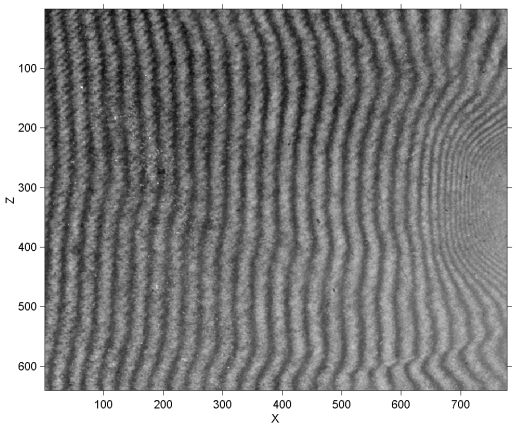

Figure 13: *A sample interferogram (***Int 1***) of a plasma produced by laser explosion of a* $0.5\mu m$ *thick,* $400\mu m$ *diameter Aluminium dot coated onto a* $0.1\mu m$ *plastic stripe support. The interferogram was taken* $3.0ns$ *after the peak of the plasma forming pulses using a modified Nomarski interferometer. The intensity on target was* $8.5 \times 10^{13} W/cm^2$*. The probe pulse-length was* $100ps$ *and the probe wavelength was* $0.53\mu m$*. For details on the experimental set-up see [6]*

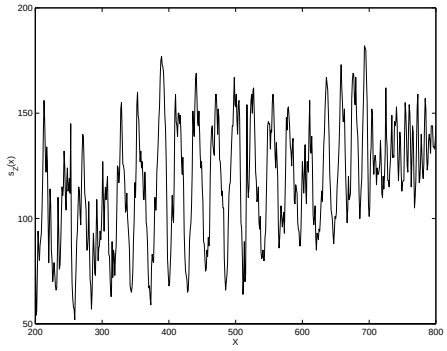

Figure 14: *A section of the interferogram* **Int 1** *at* $Z = 400$ *(***bulk***).*

tions sharply reduces for $x \approx 700$ (this phenomenon is known as "reduction of fringe visibility", see [6]).

The FFT-based phase-shift extraction uses FFT for both filtering the sequence from noise and background (with cuts in the spatial frequency domain introduced by hand) and extracting the phase by using straightforward FFT coefficients manipulations [6].

3.2 The *IACRE* phase-shift estimation: an introduction

To introduce the *IACRE* method to extract the phase-shift, let us observe that the sequence s_Z (and generally each sequence $I(z = Z, x)$) has the same structure of the signal s_2, that is a frequency-modulated sequence plus some corrections (noise, slowly varying background). It is then therefore natural to try to extract the s_Z phase-shits by using CWT techniques, with Ridge detection playing a relevant role.

Consider the CWT map of the sequence s_Z @$Z =$ 400 (see Fig. 15); its aspect is similar to the CWT map of the s_2 signal (Fig. 8), apart from the presence of a background and a reduction of the Ridge intensity for $x \approx 700$. We can then try to apply the Ridge-extraction technique to the CWT map of s_Z to both denoise the sequence and extract the phase for each pixel position x. The Ridge sequence will be constituted by only the frequency-modulated components of s_Z, so that noise and background will be automatically discarded. This is the case for s_Z @$Z = 400$, as it is clear in Fig. 16 and in the zoom on the right hand tail (Fig. 17). The phase sequence $\phi_Z(x)$ for the analyzed array s_Z is then simply computed as the

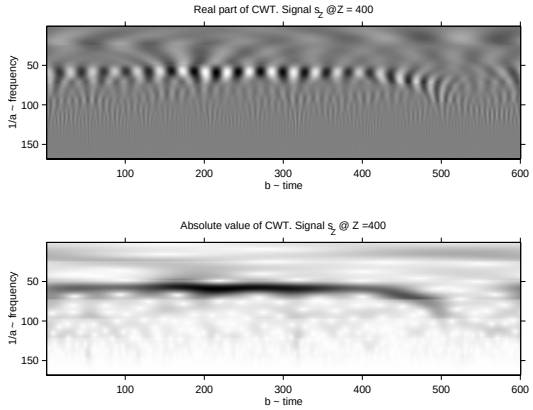

Figure 15: *The real part and absolute value CWT maps of a signal* s_Z @ $Z = 400$ *(interferogram* **Int 1** *with Morlet Mother Wavelet.*

phase of the complex sequence of CWT at the Ridge:

$$\phi_{s_Z}(x) \equiv phase\left((W_{s_Z})(x, a_R(x))\right) , \qquad (3.12)$$

and the phase-shift $\Delta\phi_{s_Z}(x)$ is obtained as

$$\Delta\phi_{s_Z}(x) \equiv \phi_{s_Z}(x) - \phi_0(x) , \qquad (3.13)$$

where $\phi_0(x) = k_p\, x$ and k_p is the wavenumber of the not-perturbed fringes.

3.3 The *IACRE* method step-by-step

Let us now examine the recipe for the *IACRE* algorithm. Let $I(z, x)$ be the gray-level image matrix of dimension $M \times N$. The first steps are the estimation of the unperturbed fringe wavelength k_p and (eventually) image filtering to slightly reduce noise. Next for each $Z \in [1\, M]$ we consider the sequence

$$s_Z(x) \equiv I(z = Z, x) \ , x \in [1\, N]$$

and:

- **Compute the (complex) CWT map**

  $$W_Z(a, b)$$

  with the Morlet base in the Log sampling. To do this one must choose the number of voices per octave N_v. A large N_v ($N_v > 12$) should be

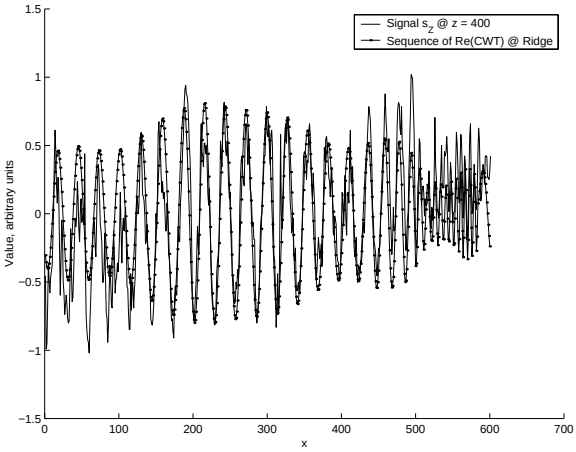

Figure 16: *The sequence of real part of CWT map of signal* s_Z@$Z = 400$ *(Interferogram* **Int 1***) with Morlet Mother Wavelet @ Ridge.*

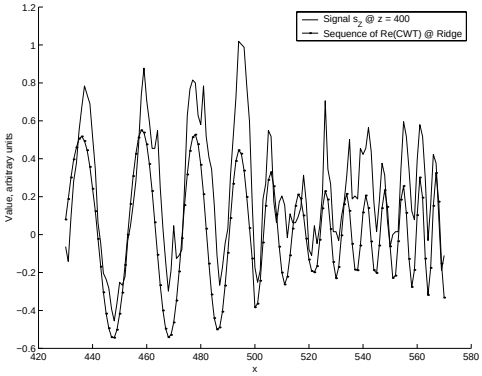

Figure 17: *The sequence of real part of CWT map of signal* s_Z@$Z = 400$ *(Interferogram* **Int 1***) with Morlet Mother Wavelet @ Ridge. Zoom on the right hand tail.*

preferred if fast changes in the local frequency $\Omega(x)$ are expected. In addition, if we expect that in some regions the local frequency $\Omega_Z(x)$ could have abrupt changes (local irregularities, structures, edges ...), a higher spatial resolution is preferred ($\omega_0 = 2\pi$, $\tau < 1$), while for regular behaviour (like the one of interferogram *Int 1*) a medium space-frequency resolutions should be used ($\tau = 1$).

- **Detect the (complex) Ridge sequence** $R_Z(x) \equiv W_{s_Z}(x, a_R(x))$.
- **Compute the phase of** R_Z:

$$\phi_Z(x) = phase(R_Z(x)) .$$

- **Estimate the phase-shift at** $z = Z$ **as**

$$\delta\phi(Z, x) \equiv \phi_Z(x) - k_p . x$$

The result is a phase-shift matrix $\delta\phi(z, x)$ of dimension $M \times N$. Phase unwrapping algorithms are then applied to the phase-shift map to eliminate unphysical phase jumps (this is the case for FFT-based results too).

3.4 *IACRE* results *versus* FFT-based results

In this section we compare the robustness of the two methods with respect to noise and other interferometric image imperfections. To start, we apply the *IACRE* method to the whole interferometric image of Fig. 13, which is corrupted from noise, strong reduction of fringe visibility and the presence of small scale periodical structures not related to the plasma properties. The first result is obtained with the *undenoised image* and $N_v = 12$ voices per octave (low N_v). The phase shift map is shown in Fig. 18, which should be compared with the FFT-method phase-shift of Fig. 19, while in Fig. 20 the line out's of the two phase shift maps @$X = 700$ are reported. As is clear from the figures, the *IACRE* method succeeds in generating a clear phase-shift map for the unfiltered image Fig. 13, while with the FFT-based method the output is unsatisfactory because it presents several unphysical phase jumps.

In the next two figures Fig. 21 and Fig. 22 we compare the performances of CWT and FFT based

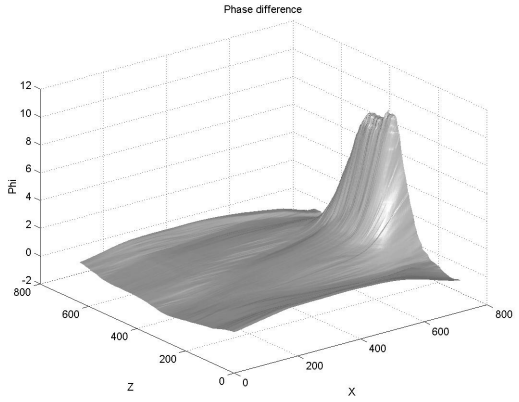

Figure 18: *The phase-shift map (in 2π units) of the non filtered* **Int 1** *image (see Fig. 13).* **CWT method**.

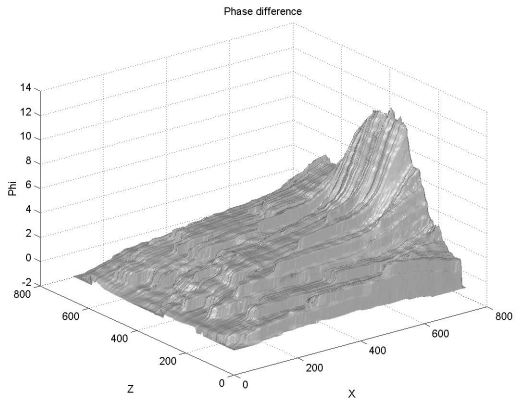

Figure 19: *The phase-shift map (in 2π units) of the non filtered Int 1 image (see Fig. 13).* **FFT method**.

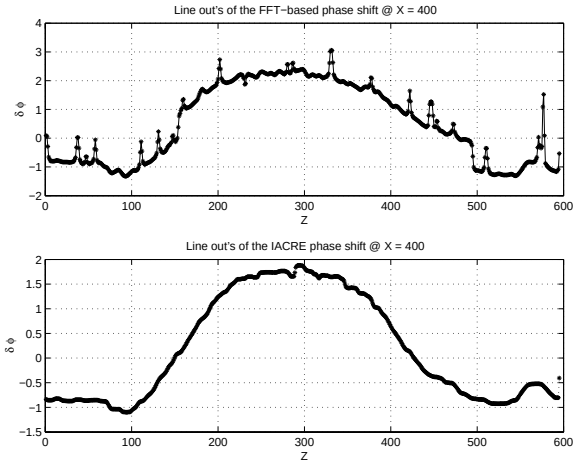

Figure 20: *Line out's of the phase-shift maps (in* 2π *units) of the non filtered Int 1 image @*$X = 700$ *(see Fig. 13) obtained with the* **FFT-based** *(top) and* **IACRE** *(bottom) methods. While the* **IACRE** *output is a continuous sequence, the FFT-based one is full of (unphysical) phase jumps which survive to phase-unwrapping procedures.*

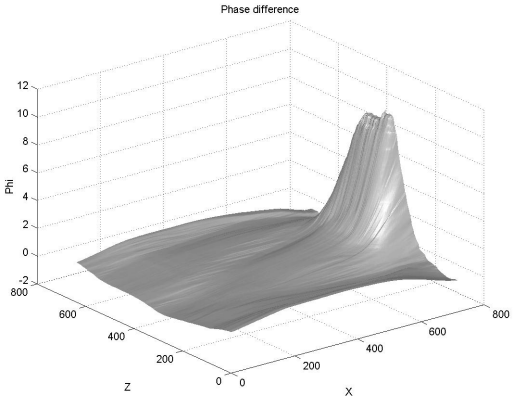

Figure 21: *The phase-shift map (in* 2π *units) of the of the Median-filtered* (3×3)*+ Wiener-filtered* (5×5) **Int 1** *image (see Fig. 13).* **CWT method**

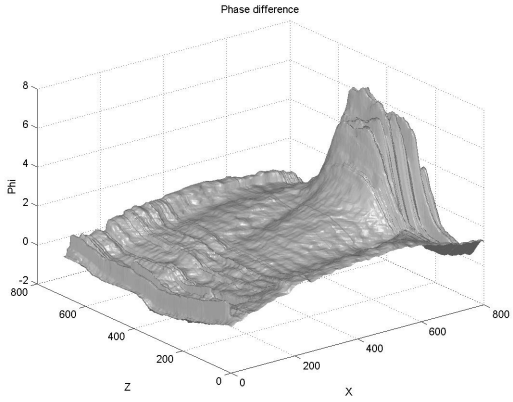

Figure 22: *The phase-shift map (in* 2π *units) of the Median-filtered* (5×5) *+ Wiener-filtered* (5×5) **Int 1** *image (see Fig. 13).* **FFT method**

methods for the same interferogram *now partially filtered from noise* with a Median-Filter of mask size 3×3 pixels followed by a Wiener-Filter 5×5. While the CWT output seems to be good (and basically identical to the not denoised image), FFT output still remain noisy and not satisfying due to the presence of (not physical) phase jumps.

Let us apply the methods to a different interferogram (see Fig. 23 for interferogram *Int 2*). As before, the first two results are obtained with a not filtered image (see images Fig. 24 and Fig. 25), while figures Fig. 26 and Fig. 27 show the results for the 5×5 median-filtered image Fig. 23. Figures Figg. 24, 25, 26, 27 show that, while the *IACRE* output is a continuous map in both the not filtered and the filtered images, the FFT-based output is noisy and not free from phase jumps. This behaviour for the FFT-b output is caused by a strong presence of noise, which could not be completely removed preserving the fringe structure. Instead, the noise seems not disturb the *IACRE* phase-shift computation which produces reasonable results even with the not denoised image.

To end the comparison between the CWT and FFT based approaches, let us apply the methods to a third interferogram *Int 3* (see Fig. 28), in which

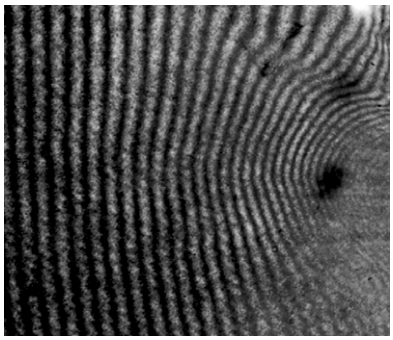

Figure 23: *A sample interferogram* **Int 2** *obtained in similar conditions as* **Int 1** *but with the probe pulse reaching the plasma at a later time* $(4.3ns)$.

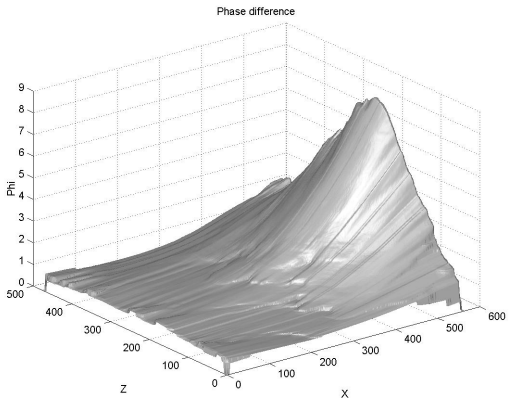

Figure 24: *The phase-shift map (in* 2π *units) of the of the unfiltered* **Int 2** *image Fig. 23.* **CWT method**

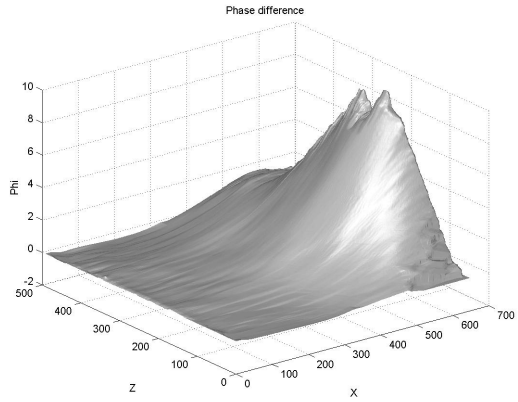

Figure 26: *The phase-shift map (in* 2π *units) of the of the Median-filtered* (5×5) **Int 2** *image Fig. 23.* **CWT method**

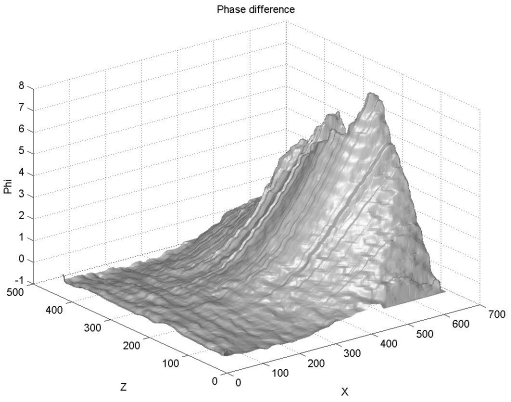

Figure 25: *The phase-shift map (in* 2π *units) of the not filtered* **Int 2** *image Fig. 23.* **FFT method**

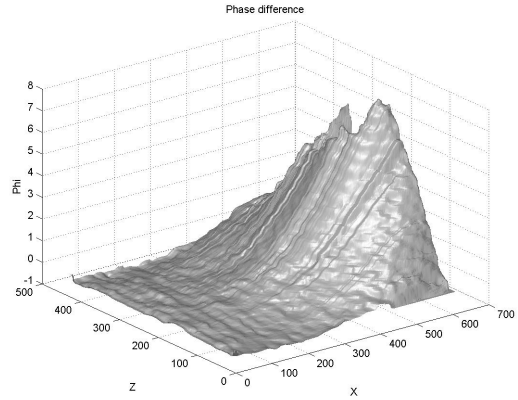

Figure 27: *The phase-shift map (in* 2π *units) of the Median-filtered* (5×5) **Int 2** *image Fig. 23.* **FFT method**

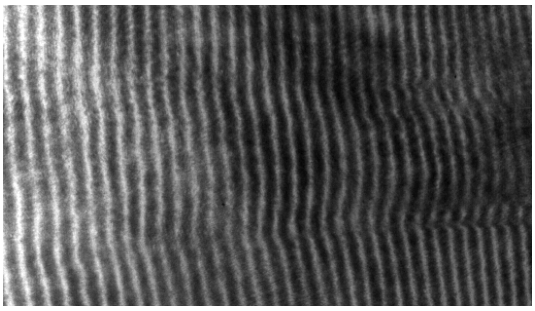

Figure 28: *A sample interferogram* **Int 3** *of a channel in a preformed plasma generated by ultra-relativistic laser-plasma interactions with preformed plasmas. The preformed plasma was generated using a similar technique as in the case of* **Int 1**. *A relativistically intense laser pulse is then focused in the preformed plasma where it creates a density channel [8]. The probe pulse in this case was* $1ps$ *pulselength* $0.25\mu m$ *wavelength and was timed to reach the plasma* $40ps$ *after the channel forming pulse*

localized effects due to a plasma channel formation are under investigation.

The four images Figg. 29, 30, 31 and 32 are referred to the phase-shift maps of the not filtered image Fig. 28 and the 3×3 Median filtered $+$ 5×5 Wiener filtered image.

From figures Figg. 30 and 32 we can see that the FFT outputs of *Int 3* are satisfying (no unphysical phase jump is present) but still noisy, while in the *IACRE* outputs (Figg. 29 and 31) the noise seems to be reduced even in the not-denoised image. We will address the problem of a detailed comparison between the *sensibility* (and consequently the noise content of the phase maps) of the two methods in the next paragraph.

Let us conclude this section with some comments about *IACRE* and FFT-based behaviours with sub-optimal images:

- The application of the FFT-based technique to unfiltered (noisy) images led to fully unsatisfactory results for interferogram *Int 1*. For this image the application of quite strong noise removal filters no not considerably improved the FFT-based outputs. The interferogram *Int 2* FFT-based phase-shift maps seems to be more robust than the output of *Int 1*, but unphys-

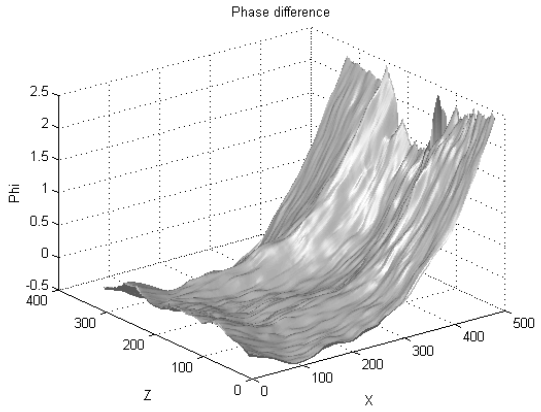

Figure 29: *The phase-shift map (in* 2π *units) of the not filtered* **Int 3** *image Fig. 28.* **CWT method**

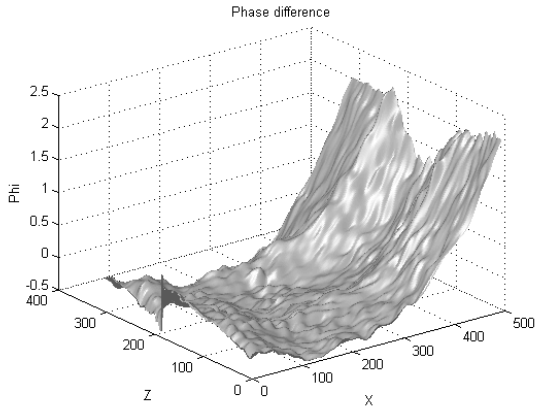

Figure 30: *The phase-shift map (in* 2π *units) of the not filtered* **Int 3** *image Fig. 28.* **FFT method**

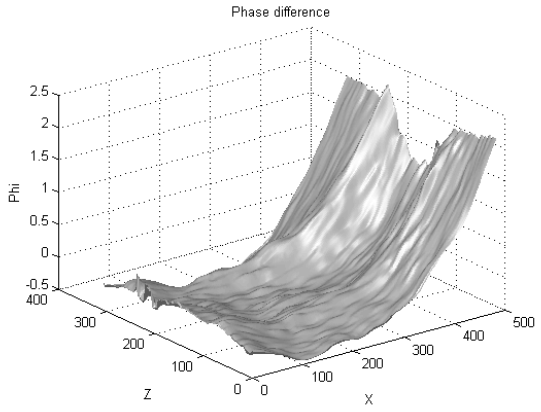

Figure 31: *The phase-shift map (in* 2π *units) of the Median-filtered* (3×3) *+ Wiener filtered* 5×5 **Int 3** *image Fig. 28.* **CWT method**

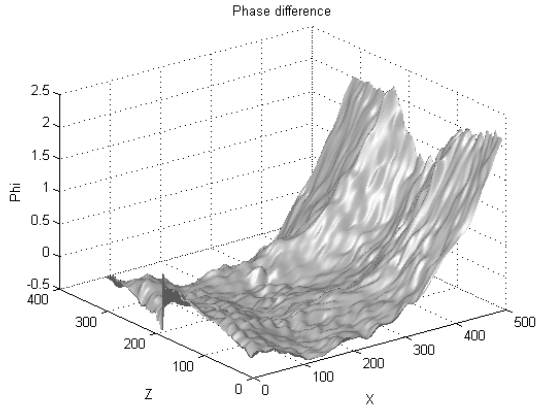

Figure 32: *The phase-shift map (in 2π units) of the Median-filtered (3×3) + Wiener filtered 5×5* **Int 3** *image Fig. 28.* **FFT method**

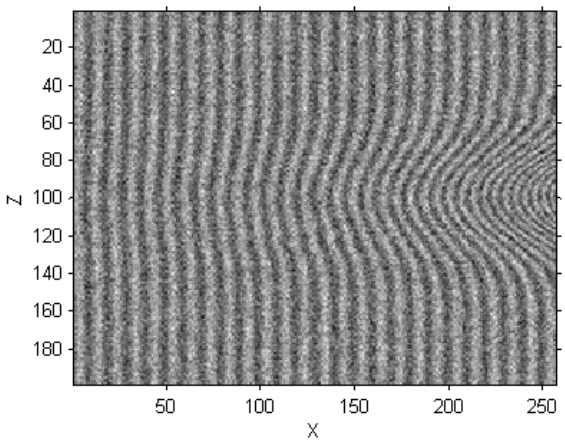

Figure 33: *A simulated interferogram* **Sim1** *of a plasma containing three small filaments.*

ical phase jumps survive to phase-unwrapping procedure. The FFT-based output of interferogram *Int 3* is robust with both the unfiltered and the filtered images, but strongly noisy.

- For all the three interferograms *IACRE* phase-shift maps are satisfying and much less noisy than the corresponding FFT-based outputs. With the exception of the interferogram *Int 2*, no relevant output improvement is obtained with the prior application of denoising filters to the input images: for most of the images no denoising is needed, **thus saving morphological informations from filtering blurring and other image deformations produced by both linear and non-linear filtering**.

3.5 Comparison between the *IACRE* and FFT-based accuracy performances

In this section we will face the second main aspect of the *IACRE* method: **the higher accuracy** with respect to the FFT-based one. We stress now that this is a very important characteristics of our procedure, since it enables an accurate search of small non-uniformity of the phase-shift map which are important to detect the growth of plasma instabilities as filamentation and self-focusing.

To this purpose, we numerically build-up two interferograms in which we simulate the phase shift produced by a slowly-varying background (the second which approximates the early stages of the preformed plasma expansion and the first which approximates the intermediate stages) plus some small scale filaments. Noise and reduction of fringe visibility are finally added to the interferometric image to better match the real interferograms characteristics. The interferogram **Sim1** (see Fig. 33) simulates a plasma with a background of maximum electronic density $(n_e/n_c)_{Max} = 0.1$ with a gaussian profile in the radial direction (with radius $75\mu m$) which is exponentially decreasing in the x direction. Three filaments are then added in different positions, with gaussian density profiles:

$$\frac{\delta n(x,y,z)}{n_c} = \alpha \exp(-(\sqrt{z^2+y^2}/r)^2)$$

with maximum density perturbation and radius ($\alpha = 0.005, r = 10\mu m$), ($\alpha = 0.005, r = 8\mu m$) and ($\alpha = 0.005, r = 6\mu m$) respectively. Since the electronic density is everywhere much lower than the critical density, the linearity of the phase map with respect to the density is respected. We can then compute the perturbation of the phase-shift map in 2π units ($\phi_{2\pi} \equiv \phi/(2\pi)$) with respect to the background as

$$\delta(\Delta\phi_{2\pi}) = -\frac{1}{2\lambda_p}\int \frac{\delta n}{n_c} dy\,,$$

whose maximum value is

$$\delta(\Delta\phi_{2\pi})_{Max} = \frac{1}{2}\sqrt{\pi}\alpha\frac{r}{\lambda_p}\,, \qquad (3.14)$$

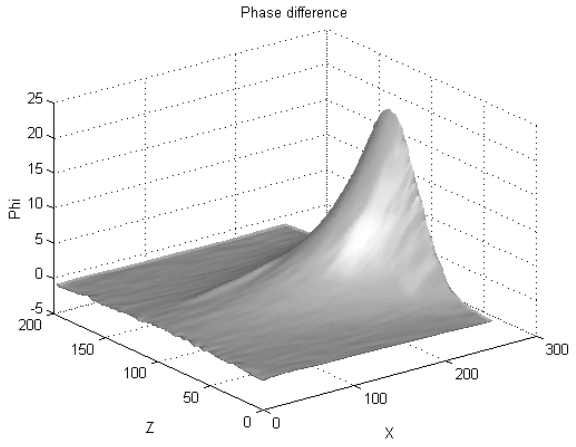

Figure 34: *Phase-shift map of the interferogram* **Sim1**. **IACRE** *method.*

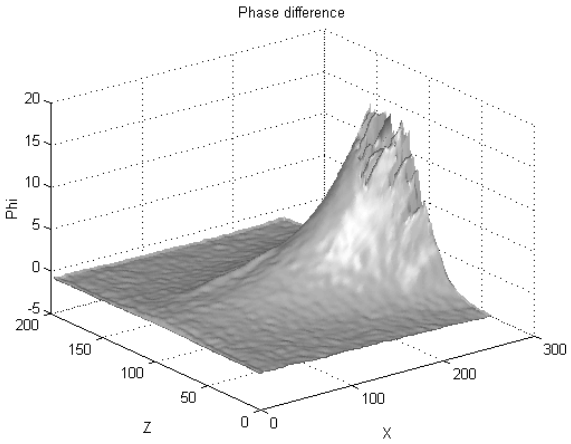

Figure 35: *Phase-shift map of the interferogram* **Sim1**. **FFT-based** *method .*

that is $\delta(\Delta\phi_{2\pi})_{Max} = 0.18$, $\delta(\Delta\phi_{2\pi})_{Max} = 0.14$ and $\delta(\Delta\phi_{2\pi})_{Max} = 0.11$, respectively. To detect these structures, the noise level of the phase-shift map should be a fraction of $\delta(\Delta\phi_{2\pi})_{Max}$. If $\sigma(x)$ is the standard deviation of the noise of each sequence of $\Delta\phi_{2\pi}(z,x)$ at x fixed, we could detect these structures if their amplitudes are for instance at "two sigma" with respect to the noise, that is $\sigma(x) < 0.09$, $\sigma(x) < 0.07$ and $\sigma_x < 0.05$ respectively (clearly if two ore more structures are present at the same x the minimum of $\delta(\Delta\phi)$ should be considered). The standard deviation $\sigma(x)$ (or one fraction of $\sigma(x)$) could be then be considered as a rough estimation of the "detectable threshold" in the phase-shift map".

To estimate the accuracy of the phase-shift maps obtained with the *IACRE* and FFT-based methods, we compute the phase-shift maps with the two methods (see Figg. 34 and 35) and we compare them with the known "true" phase map. We start the analysis by comparing some line-out of the two phase maps with the known simulate map. In Fig. 36 it is clear that the noise in the two phase maps is comparable in regions of the interferogram with low phase-shift, while for large phase-shifts the FFT-based output clearly fail in producing an accurate phase map.

More precise statements are possible since the exact value of the phase-shift map is known. Denoting with $\Delta\phi_{2\pi}^{CWT}$ and $\Delta\phi_{2\pi}^{FFT}$ the phase-shits maps obtained with the two methods and with $\Delta\phi_{2\pi}^{Thrue}$ the

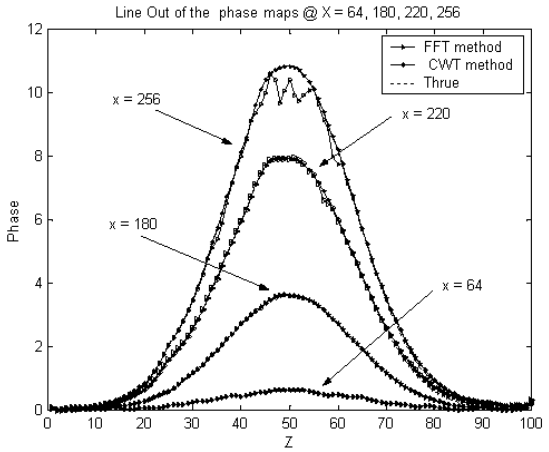

Figure 36: *Line-out of the phase-shift maps of the interferogram* **Sim1**. *The* **IACRE** *and* **FFT-based** *methods outputs are compared with the 'true' simulated map*

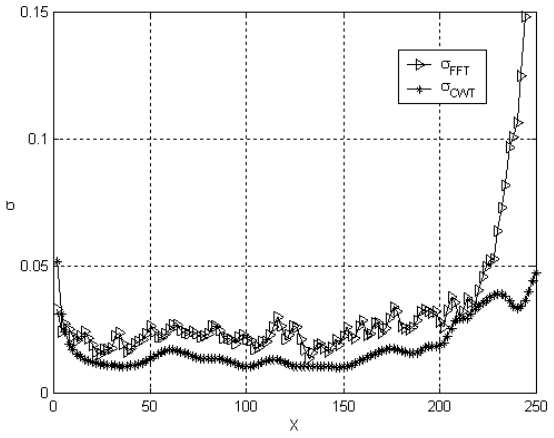

Figure 37: *Standard deviations of the error in the phase-shift map of interferogram* **Sim1** *computed via IACRE and FFT-based methods.*

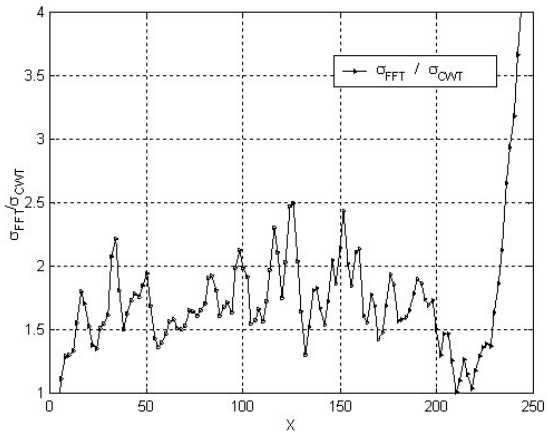

Figure 38: *Ratio between the standard deviations of the error in the phase-shift map of interferogram* **Sim1** *computed via FFT-based and IACRE methods. For density perturbations δn with gaussian density profile in the z direction of amplitude α and radius r, the sequence $\sigma_{FFT}/\sigma_{CWT}$ can also be interpreted as the ratio between the* **minimum** *product $(\alpha\, r)$ detectable with the FFT-based and IACRE methods: $\sigma_{FFT}/\sigma_{CWT} \sim (\alpha\, r)^{Min}_{FFT}/(\alpha\, r))^{Min}_{CWT}$*

simulated phase map, the estimations of the error map are computed as the differences:

$$\begin{aligned} \mathcal{E}_{CWT}(z,x) &\equiv \Delta\phi^{CWT}_{2\pi}(z,x) - \Delta\phi^{Thrue}_{2\pi}(z,x)\,, \\ \mathcal{E}_{FFT}(z,x) &\equiv \Delta\phi^{FFT}_{2\pi}(z,x) - \Delta\phi^{Thrue}_{2\pi}(z,x)\,, \end{aligned}$$

so that the sequences of the standard deviations of the noise in the phase map can be estimated as

$$\begin{aligned} \sigma_{FFT}(x) &= std(\mathcal{E}_{FFT}(z,x))\,, \\ \sigma_{CWT}(x) &= std(\mathcal{E}_{CWT}(z,x))\,, \end{aligned} \qquad (3.15)$$

where $std(f(z))$ is the standard deviation of a sequence $f(z)$.

In Fig. 37 is shown the behaviour of the error in both the *IACRE* and FFT-based maps, while in Fig. 38 the ratio $R(x)$ between $\sigma_{FFT}(x)$ and $\sigma_{CWT}(x)$ sequences is reported. The analysis of these figures confirms the claim that in small phase-shifts regions the *IACRE* method exhibits a slightly higher precision than the FFT-based one (the $\sigma_{FFT}/\sigma_{CWT}$ sequence is the interval $1.3 - 2.5$), while in large phase-shift regions the sensibility of the *IACRE* method is much higher than the one of the FFT-based one. For example, assuming the sequence $\sigma(x)$ as an estimation of the phase-shift sensibility, since for gaussian density profiles $\delta(\Delta\phi_{2\pi})_{Max}$ is proportional to the structure radius r and the maximum density perturbation α (see 3.14), the sequence $R = \sigma_{FFT}/\sigma_{CWT}$ could be interpreted as a rough estimation of the ratio between the **minimum** product $\alpha\, r$ detectable with the FFT-based and *IACRE* techniques:

$$R \equiv \frac{\sigma_{FFT}}{\sigma_{CWT}} \sim \frac{(\alpha\, r))^{Min}_{FFT}}{(\alpha\, r))^{Min}_{CWT}}\,.$$

Futhermore, since for the *IACRE* method the σ_{CWT} sequence is everywhere below the value 0.04 (see the "detection thresholds" reported above), we are confident that all the three filaments could be detected. This is not the case for the FFT-based method output because in the region $X \in [220, 250]$ the σ_{FFT} sequence is in the range $0.05 - 0.15$, which is over the minimum of the detection thresholds.

We conclude the analysis of the interferogram **Sim1** by checking the behaviour of the phase maps when an algorithm for the automatic extraction of small scale perturbations is applied to the phase-shift maps. The algorithm utilized is very simple and consists of two main steps:

- The decomposition of the map $\Delta\phi_{2\pi}$ in a 'Large scale' component (the background) $\bar{\Delta\phi}_{2\pi}$ and a 'Small scale' component $\delta(\Delta\phi_{2\pi})$ (the struc-

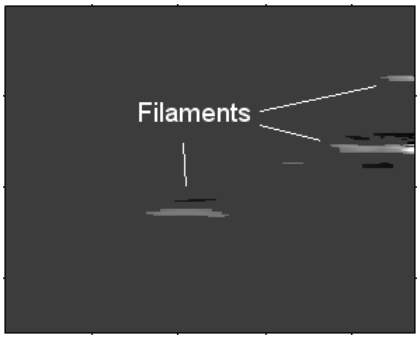

Figure 39: *Filtered map at "two sigma" of the 'Small scale' component of the phase-shift map of interferogram* **Sim1** *computed via IACRE methods. Three filaments are clearly detected.*

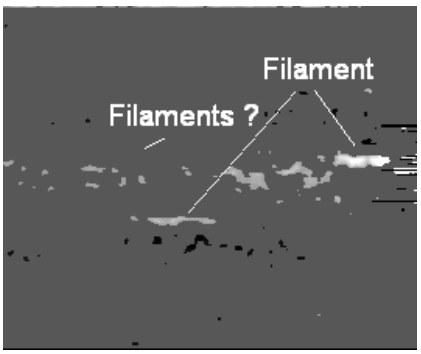

Figure 40: *Filtered map at "two sigma" of the 'Small scale' component of the phase-shift map of interferogram* **Sim1** *computed via FFT-based methods. Two filaments could be detected but other unreal structures survive to the "two sigma" filter.*

tures + noise) by using a Smoothing B-spline fitting for each line-out of the phase map at x fixed.

- The filtering of the small scale component $\delta(\Delta\phi_{2\pi})$ with a "two sigma" cutoff. As explained before, provided that structures in the $\delta(\Delta\phi_{2\pi})$ give a negligible contribution in the Root-Mean-Square of the map, the standard deviations $\sigma_{FFT}(x)$ and $\sigma_{FFT}(x)$ can be computed as

$$\begin{aligned} \sigma_{FFT}(x) &= std(\delta(\Delta\phi_{2\pi}^{FFT})(z,x))\,, \\ \sigma_{CWT}(x) &= std(\delta(\Delta\phi_{2\pi}^{CWT})(z,x)) \end{aligned} \tag{3.16}$$

In Figg. 39 and 40 the filtered at "two sigma" 'Small scale' phase maps obtained with the two methods are reported. As expected, the filtered map of the *IACRE* method clearly shows the presence of the three filaments, while in the FFT-based map some regions of the map with strong presence of noise could be interpreted as *false* small scale structures so no clear filaments detection is possible.

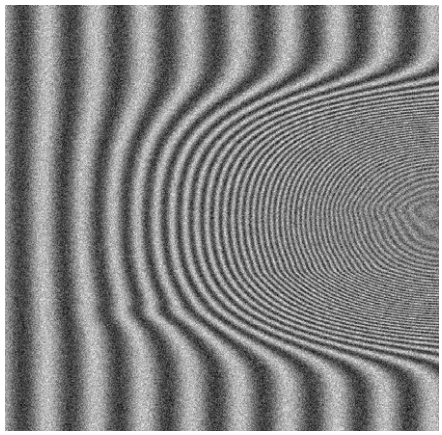

Figure 41: *A simulated interferogram* **Sim2** *of a plasma containing three small filaments.*

Let us analyze now a second simulated interferogram **Sim2** (see Fig. 41), with a background of maximum density profile $(n_e/n_c)_{Max} = 0.25$, a gaussian profile in the x direction and a super-gaussian of power four, e.g

$$\delta n_e/n_c \sim \alpha exp(-((y^2+z^2)^2/r^4)$$

in the radial direction. As before, three small filaments with gaussian radial profile are added now with density perturbation **with respect to the background** of maximum relative value

$$\beta \equiv (\delta n/n_{Background})_{Max}$$

and spatial scale r of $(\beta = 0.05\,, r = 8\mu m)$, $(\beta = 0.05\,, r = 10\mu m)$ and $(\beta = 0.025\,, r = 10\mu m)$ respectively.

The phase-shifts maps obtained with the two methods are shown in Figg. 42 and 43, which reveal immediately that, apart from a very thin band $@Z \approx 180$, the FFT-based method now succeed in producing a phase map free from unphysical phase-jumps.

The comparison between accuracy performances of the two methods can be obtained as before by checking the behaviours of the standard deviations of the errors $\mathcal{E}_{CWT}$ and $\mathcal{E}_{FFT}$ (see 3.15), which are reproduced in Figg. 44 and 45. As for the interferogram

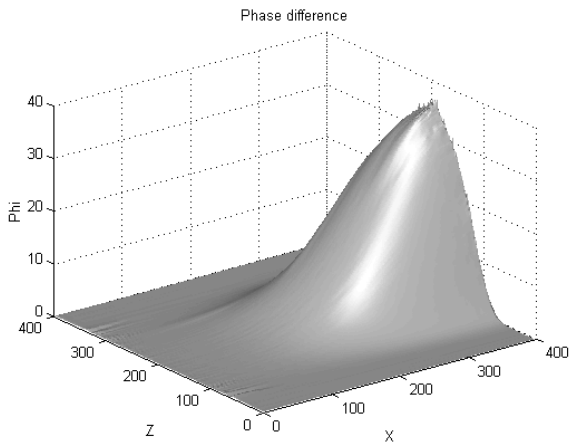

Figure 42: *Phase-shift map of the interferogram* **Sim2**. **IACRE** *method.*

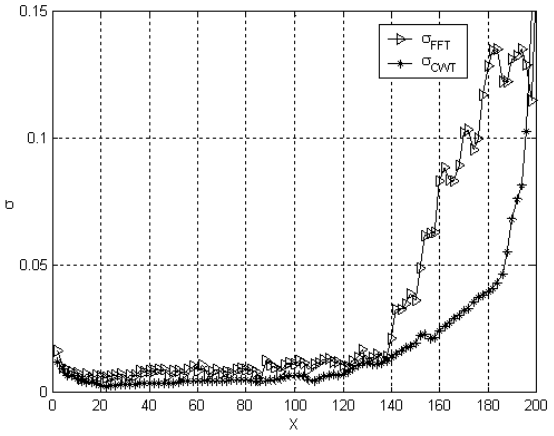

Figure 44: *Standard deviations of the error in the phase-shift map of interferogram* **Sim2** *computed via IACRE and FFT-based methods.*

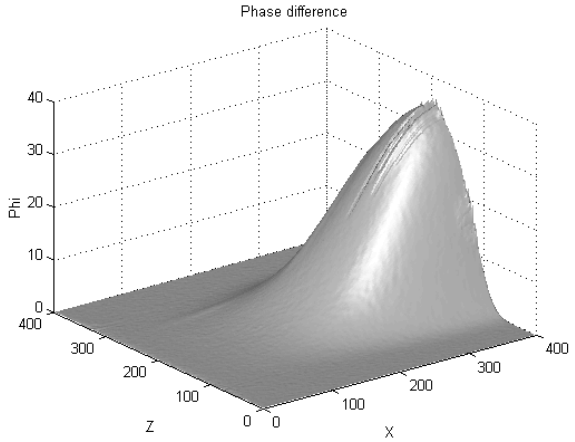

Figure 43: *Phase-shift map of the interferogram* **Sim2**. **FFT-based** *method .*

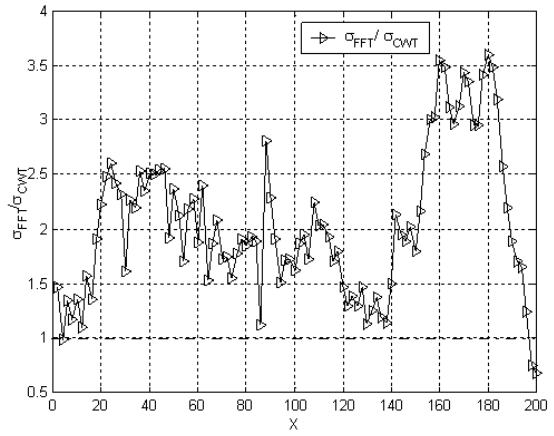

Figure 45: *Ratio between the standard deviations of the error in the phase-shift map of interferogram* **Sim2** *computed via FFT-based and IACRE methods. For density perturbations δn with gaussian density profile in the z direction of amplitude α and radius r, the sequence $R(x) \equiv \sigma_{FFT}(x)/\sigma_{CWT}(x)$ can also be interpreted as the ratio between the* **minimum** *product $\alpha \dot{r}$ detectable with the FFT-based and IACRE methods: $\sigma_{FFT}/\sigma_{CWT} \sim (\alpha\, r)^{Min}_{FFT}/(\alpha\, r)^{Min}_{CWT}$*

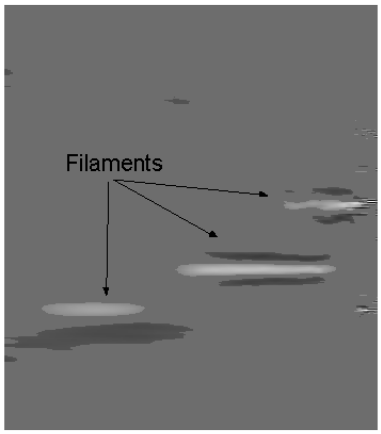

Figure 46: *Filtered map at "two sigma" of the 'Small scale' component of the phase-shift map of interferogram* **Sim2** *computed via IACRE methods. Three filaments are clearly detected.*

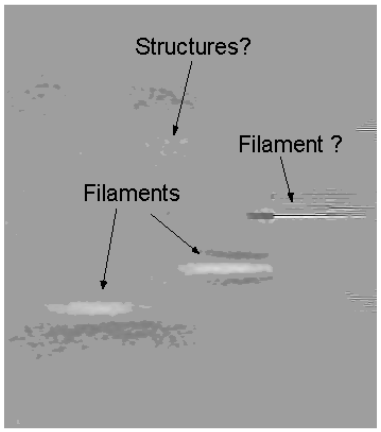

Figure 47: *Filtered map at "two sigma" of the 'Small scale' component of the phase-shift map of interferogram* **Sim2** *computed via FFT-based methods. Two filaments are detected but some other unreal structures survive to the filtering procedure.*

Sim1 we claim that the sensibility of the **IACRE** method for **Sim2** is locally $R(x)$ times the one of FFT-based one. The minimum detectable structures are then such that

$$(\alpha\, r)^{Min}_{CWT}(x) \approx \frac{1}{R(x)}(\alpha\, r)^{Min}_{FFT}(x)$$

with $R(x)$ as in Fig. 45, therefore, as for **Sim 1**, the two methods have slightly different sensibilities in low density plasma regions, while in relatively dense plasma zones the *IACRE* method is much more accurate.

We conclude the analysis of interferogram **Sim2** by comparing the "two sigma" filtered 'Small scale' phase maps computed with the same procedure of the interferogram **Sim1** (see eq. 3.16). In Figg. 46 and 47 the filtered 'Small scale' phase-shift maps are reported. The results clearly show that the *IACRE* map accuracy is sufficient to detect the three filaments, while in the FFT-based map the filament on the top-right of the phase image is not clearly detected and in addition not physical structures survive to the "two sigma" filter.

4 Conclusions

From the compared analysis of the *IACRE* and FFT-based methods emerged that:

- **Robustness.** The *IACRE* method is generally more robust than the FFT-based one, particularly when very low quality (strongly noisy, relevant lowering of fringe visibility) images are analyzed. In addition, the *IACRE* method often succeed in producing a correct phase-shift map without a prior smoothing of the interferometric image. This is an important goal of the procedure, because almost all of the linear and non-linear noise-removal filters introduce blurring and other deformations in the image, which could change the small-scale details of the phase map.
- **Sensibility.** With the help of two simulated interferograms we showed that the *IACRE* method is more accurate than the FFT-based one. For those interferograms the smallest detectable phase-shift perturbation (with respect to the background) obtained with the *IACRE* method is in the mean 0.5 times the one obtained with the FFT-based one, with possible strong decrease

in large density regions.

In a next paper we will apply the *IACRE* method in a systematic analysis of a sequence of interferograms with and without a preformed channel (as interferograms **Int 3**), with the aim of achieve both a good characterization of the channel profiles and a detection of small-scale density fluctuations.

Acknowledgments

The authors wish to acknowledge support from the italian M.U.R.S.T. (Project: "Metodologie e diagnostiche per materiali e ambiente"). One of us (PT) would also thank Guido Buresti (University of Pisa) and Elena Cuoco (I.N.F.N, section of Firenze/Urbino) for useful discussions on Continuous Wavelet Transform.

References

[1] M.G.Nomarski, Journal de la Physique et le Radium **16**, 95 (1955)

[2] R.Benattar, C.Popovics, R.Siegel Rev.Sci.Instrum. **50**, 1583 (1979)

[3] O.Willi, in Laser-Plasma Interaction 4, Proceedings of XXXV SUSSP, St.Andrews, 1988

[4] M.Takeda, H.Ina, S.Kobayashi, J.Opt.Soc.Am. **72**, 156 (1982).

[5] K.A.Nugent, Applied Optics **18**, 3101 (1985)

[6] L.A.Gizzi et al., Phys.Rev. E, **49**, 5628 (1994)+ Erratum Phys.Rev. E, **50**, 4266 (1994)

[7] M. Borghesi et al., Phys.Rev. E, **54**, 6768 (1996)

[8] M. Borghesi et al., Phys.Rev.Lett., **78**, 879 (1997)

[9] D. Gabor; *Theory of Communication*, J. Inst. Electr. Eng., London, 93 (III), pp 429-457

[10] J. Morlet, G. Arens, I. Fourgeau and D. Giard; *Wave propagation and sampling theory*, Geophysics, **47**, pp. 203-236

[11] M. Holschneider; *Wavelet: An analysis tool*, Clarendon Press -Oxford (1995)

[12] I. Daubechies; *Ten lectures on Wavelets*, Soc. for Ind. and Applied Mathematics, Philadelphia (1992)

[13] R. Carmona, W.L. Hwang and B. Torresani; *Characterization of Signals by the Ridges of their Wavelet Transform.* paper; IEEE Trans. Signal Processing **45**, vol. 10, p. 2586.

[14] B. Torresani; *Time Frequency and Time Scale Analysis*, abstract in Signal Processing for Multimedia, J. Byrnes Ed. (1999) p. 37-52.

[15] J.M. Innocent and B. Torresani; *A Multiresolution Strategy for Detection Gravitational Waves Generated by Binary Coalescence*, Submitted to Phys. Rev. D

[16] P. Tomassini, A. Giulietti and L.A. Gizzi; Analyzing laser-plasma interferograms with the continuous Wavelet Transform, **IFAM-Note** 2/2000, 15-11-2000, avaible in PDF format @ http://xray.ifam.pi.cnr.it/Group/Referencesrev.html.